arXiv:1403.3863v1 [math.NA] 16 Mar 2014

REGULARIZED SOLUTION OF A NONLINEAR PROBLEM IN ELECTROMAGNETIC SOUNDING

GIAN PIERO DEIDDA*, CATERINA FENU†, AND GIUSEPPE RODRIGUEZ†

1. Introduction. Electromagnetic induction measurements are often used for non-destructive investigation of certain soil properties, which are affected by the electromagnetic features of the subsurface layers, e.g., the electrical conductivity and the magnetic permeability. Knowing such parameters allows one to identify inhomogeneities in the ground, and to ascertain the presence and the spatial position of particular conductive substances, such as metals, liquid pollutants, or saline water. This leads to important applications in Geophysics [4, 8, 17, 24], Hydrology, [16, 21], Agriculture [5, 9, 26], etc.

A ground conductivity meter (GCM) is a rather common device for electromagnetic sounding, initially introduced by the Geonics company. It is composed by two coils (a transmitter and a receiver) placed at the extrema of a bar. An alternating current in the transmitter coil produces a primary magnetic field H_P, which induces small currents in the ground. These currents produce a secondary magnetic field H_S, which is sensed by the receiver coil. A GCM has two operating positions, which produce different measures, corresponding to the orientation (either vertical or horizontal) of the electric dipole generated by the transmitter coil; see Figure 1.1. The instrument is often coupled to a GPS, so that it is possible to associate to each measurement the geographical position where it was taken. Its success is due to ease of use and a relatively low price.

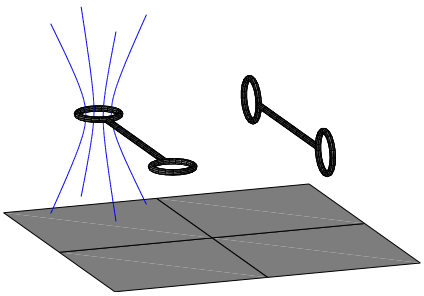

FIG. 1.1. *Schematic representation of a ground conductivity meter (GCM).*

Let us assume that the instrument is placed at ground level in vertical orientation, the soil has uniform magnetic permeability $\mu_0 = 4\pi 10^{-7}$ H/m (the permeability of free space) and uniform electrical conductivity σ. Moreover, let the *induction number* be

*Dipartimento di Ingegneria Civile, Ambientale e Architettura, Università di Cagliari, Piazza d'Armi 1, 09123 Cagliari, Italy. E-mail: gpdeidda@unica.it.

†Dipartimento di Matematica e Informatica, Università di Cagliari, viale Merello 92, 09123 Cagliari, Italy. E-mail: kate.fenu@unica.it, rodriguez@unica.it.

small

$$B = \frac{r}{\delta} = r\sqrt{\frac{\mu_0 \omega \sigma}{2}} \ll 1, \tag{1.1}$$

where δ is the *skin depth* (the depth at which the principal field H_P has been attenuated by a factor e^{-1}), r is the inter-coil distance, $\omega = 2\pi f$, and f is operating frequency of the device. In the case of the Geonics EM38 device, $r = 1\,\mathrm{m}$, $f = 14.6\,\mathrm{kHz}$, and $\delta = 10 \sim 50\,\mathrm{m}$. A GCM measures the apparent conductivity

$$m = \frac{4}{\mu_0 \omega r^2} \operatorname{Im}\left(\frac{(H_S)_d}{(H_P)_d}\right), \tag{1.2}$$

which coincides with σ under the above restrictive assumptions, where $(H_P)_d$ and $(H_S)_d$ are the components along the dipole axis of the primary and secondary magnetic field, respectively.

In real applications the assumption of uniform soil conductivity is not realistic. On the contrary, it is particularly interesting to investigate non homogeneous soils, where the electrical conductivity σ is not constant and the magnetic permeability μ may be very different from μ_0 for the presence of ferromagnetic materials.

Apparent conductivity gives no information on the depth localization of inhomogeneities. To recover the distribution of conductivity with respect to depth by data inversion, multiple measures are needed. Different measures can be generated by varying some of the parameters which influence the response of the device. As suggested in [3], we assume to place the instrument at different heights over the ground and to repeat the induction measurement with both the possible orientations.

In 1980, McNeill [18] described a linear model, based on the response curves in the vertical and horizontal positions of the device, which relates the apparent conductivity to the height over the ground. If $m^V(h)$ and $m^H(h)$ are the apparent conductivity measured by the GCM at height h, in the vertical and horizontal orientation, respectively, then

$$\begin{aligned} m^V(h) &= \int_0^\infty \phi^V(h+z)\sigma(z)\,dz, \\ m^H(h) &= \int_0^\infty \phi^H(h+z)\sigma(z)\,dz, \end{aligned}$$

where z is the ratio between the depth and the inter-coil distance r, $\sigma(z)$ is the conductivity at z, and

$$\phi^V(z) = \frac{4z}{(4z^2+1)^{3/2}}, \qquad \phi^H(z) = 2 - \frac{4z}{(4z^2+1)^{1/2}}.$$

The linear model is valid for uniform magnetic permeability μ_0, small *induction number* B, and moderate conductivity ($\sigma \lesssim 100\,\mathrm{mS/m}$). This model is not accurate when the conductivity of some subsurface layers is large. In this case a nonlinear model is available [15, 25], which will be described in the next section.

The two models are analyzed in [3, 15]. One of the conclusions is that, even if the nonlinear model produces better results when the electrical conductivity is large, "the linear model is preferred for all conductivities since it needs considerably less computer resources". The same authors made available two Matlab packages for inversion, based on the linear and the nonlinear models, respectively; see [3, 15]. An

algorithm for the solution of the linear model based on Tikhonov regularization has been analyzed in [6].

In this paper we propose a regularized inversion procedure for the nonlinear model, based on the coupling of the damped Gauss–Newton method with truncated singular value decomposition (TSVD). We give an explicit representation of the Jacobian of the nonlinear function defining the model, and show that the computational load required by the algorithm is not large, and allows real-time processing. For this reason we think that our approach is competitive with the existing ones, and can be effectively used in the presence of highly conductive materials.

The plan of the paper is the following: in Section 2 we describe a nonlinear model which connects the real conductivity of the soil layers to the apparent conductivity, and in Section 3 we compute the Jacobian matrix of the model. The inversion algorithm is introduced in Section 4, while Section 5 describes the regularization procedure adopted in the inversion algorithm. Finally, Section 6 reports the result of numerical experiments performed both on synthetic and real data.

2. The nonlinear model. A nonlinear model which relates the electromagnetic features of the soil to the height of measurement is described in [25], and it is further analyzed and adapted to the case of a GCM in [15]. The model is derived from Maxwell's equations, keeping into account the cylindrical symmetry of the problem, due to the fact that the magnetic field sensed by the receiver coil is independent of the rotation of the instrument around the vertical axis. In the following, λ is a variable of integration which has no particular physical meaning. It can be interpreted as the ratio between a length and the *skin depth* δ.

Following [25, Chapter III], we assume that the soil has a layered structure with n layers, each of thickness d_i, $i = 1, \ldots, n$. The bottom layer d_n is assumed to be of infinite width. Let σ_k and μ_k be the electrical conductivity and the magnetic permeability of the k-th layer, respectively, and let $u_k(\lambda) = \sqrt{\lambda^2 + \mathrm{i}\sigma_k\mu_k\omega}$, where $\mathrm{i} = \sqrt{-1}$ is the imaginary unit. Then, the characteristic admittance of the k-th layer is given by

$$N_k(\lambda) = \frac{u_k(\lambda)}{\mathrm{i}\mu_k\omega}. \tag{2.1}$$

The surface admittance at the top of the k-th layer is denoted by $Y_k(\lambda)$ and verifies the following recursion

$$Y_k(\lambda) = N_k(\lambda)\frac{Y_{k+1}(\lambda) + N_k(\lambda)\tanh(d_k u_k(\lambda))}{N_k(\lambda) + Y_{k+1}(\lambda)\tanh(d_k u_k(\lambda))}, \quad k = n-1, \ldots, 1, \tag{2.2}$$

where d_k is the width of the kth layer. The recursion is initialized setting $Y_n(\lambda) = N_n(\lambda)$ at the lowest layer. Numerically, this is equivalent to start the recursion at $k = n$ with $Y_{n+1}(\lambda) = 0$.

Now let,

$$R_0(\lambda) = \frac{N_0(\lambda) - Y_1(\lambda)}{N_0(\lambda) + Y_1(\lambda)}, \tag{2.3}$$

and

$$\begin{aligned} T_0(h) &= -\delta^3 \int_0^\infty \lambda^2 e^{-2h\lambda} R_0(\lambda) J_0(r\lambda)\, d\lambda, \\ T_2(h) &= -\delta^2 \int_0^\infty \lambda e^{-2h\lambda} R_0(\lambda) J_1(r\lambda)\, d\lambda, \end{aligned} \tag{2.4}$$

where $J_0(\lambda)$ and $J_1(\lambda)$ are Bessel functions of the first kind of order 0 and 1, respectively, and r is the inter-coil distance. We prefer to express the integrals (2.4) in the variable λ, instead than $g = \delta\lambda$ as in [25]. The results obtained by Wait in [25, page 113], adapted to the geometry of a GCM, give the components of the magnetic field along the dipole axis

$$\begin{aligned}
(H_P)_z &= -\frac{C}{r^3}, \qquad (H_S)_z = -\frac{C}{\delta^3} T_0(h), \qquad \text{(vertical dipole)},\\
(H_P)_y &= -\frac{C}{r^3}, \qquad (H_S)_y = -\frac{C}{r\delta^2} T_2(h), \qquad \text{(horizontal dipole)},
\end{aligned}$$

where C is a constant; in the case of a horizontal dipole, we assume its axis to be y-directed. Substituting in (1.2), we obtain the predicted values of the apparent conductivity measurement $m^V(h)$ (vertical orientation of coils) and $m^H(h)$ (horizontal orientation of coils) at height h above the ground

$$\begin{aligned}
m^V(h) &= \frac{4}{\mu_0 \omega r^2} \operatorname{Im}(B^3 T_0(h)),\\
m^H(h) &= \frac{4}{\mu_0 \omega r^2} \operatorname{Im}(B^2 T_2(h)),
\end{aligned}$$

where B is the induction number (1.1).

Simplifying formulae, we find

$$\begin{aligned}
m^V(h) &= \frac{4r}{\mu_0 \omega} \mathcal{H}_0 \left[-\lambda e^{-2h\lambda} \operatorname{Im}(R_0(\lambda)) \right](r)\\
m^H(h) &= \frac{4}{\mu_0 \omega} \mathcal{H}_1 \left[-e^{-2h\lambda} \operatorname{Im}(R_0(\lambda)) \right](r).
\end{aligned} \tag{2.5}$$

Here we denote by

$$\mathcal{H}_\nu[f](r) = \int_0^\infty f(\lambda) J_\nu(r\lambda) \lambda \, d\lambda \tag{2.6}$$

the Hankel transform of order ν of the function $f(\lambda)$. In our numerical experiments we approximate $\mathcal{H}_\nu[f](r)$ by the quadrature formula described in [1], using the nodes and weights adopted in [15].

REMARK 2.1. The above relations (2.5) show that the apparent conductivity predicted by the model is independent of the *skin depth* δ and the *induction number* B. To our knowledge, this is the first time that this is noted.

The model just described depends upon a number of parameters which influence the value of the apparent conductivity. In particular, it is affected by the instrument orientation (horizontal/vertical), its height h over the ground, the inter-coil distance r, and the angular frequency ω.

The problem of data inversion is very important in Geophysics, when one is interested in depth localization of inhomogeneities of the soil. To this purpose, multiple measures are needed to recover the distribution of conductivity with respect to depth. In order to obtain such measures, we use the two admissible orientations and assume to record apparent conductivity at height h_i, $i = 1, \ldots, m$. This generates $2m$ data values.

In our analysis, we let the magnetic permeability take the same value μ_0 in the n layers. This assumption is approximately met if the ground does not contain ferromagnetic materials. Then, we can consider the apparent conductivity as a function

of the value of the conductivity σ_k in each layer and of the height h, and we write $m^V(\boldsymbol{\sigma}, h)$ and $m^H(\boldsymbol{\sigma}, h)$, where $\boldsymbol{\sigma} = (\sigma_1, \ldots, \sigma_n)^T$, instead than $m^V(h)$ and $m^H(h)$.

Now, let b_i^V and b_i^H be the data recorded by the GCM at height h_i in the vertical and horizontal orientation, respectively, and let us denote by $r_i(\boldsymbol{\sigma})$ the error in the model prediction for the ith observation

$$r_i(\boldsymbol{\sigma}) = \begin{cases} b_i^V - m^V(\boldsymbol{\sigma}, h_i), & i = 1, \ldots, m, \\ b_{m-i}^H - m^H(\boldsymbol{\sigma}, h_{m-i}), & i = m+1, \ldots, 2m. \end{cases} \tag{2.7}$$

Setting $\mathbf{b}^V = (b_1^V, \ldots, b_m^V)^T$, $\mathbf{m}^V(\boldsymbol{\sigma}) = (m^V(\boldsymbol{\sigma}, h_1), \ldots, m^V(\boldsymbol{\sigma}, h_m))^T$, and defining $\mathbf{b}^H$ and $\mathbf{m}^H(\boldsymbol{\sigma})$ similarly, we can write the measured data vector and the model predictions vector as

$$\mathbf{b} = \begin{bmatrix} \mathbf{b}^V \\ \mathbf{b}^H \end{bmatrix}, \quad \mathbf{m}(\boldsymbol{\sigma}) = \begin{bmatrix} \mathbf{m}^V(\boldsymbol{\sigma}, \mathbf{h}) \\ \mathbf{m}^H(\boldsymbol{\sigma}, \mathbf{h}) \end{bmatrix}, \tag{2.8}$$

and the residual vector as

$$\mathbf{r}(\boldsymbol{\sigma}) = \mathbf{b} - \mathbf{m}(\boldsymbol{\sigma}). \tag{2.9}$$

To estimate the computational complexity needed to evaluate $\mathbf{r}(\boldsymbol{\sigma})$ we assume that the complex arithmetic operations are implemented according to the classical definitions, i.e., that 2 floating point operations (*flops*) are required for each complex sum, 6 for each product and 11 for each division. The count of other functions (exponential, square roots, etc.) is given separately because it is not clear how many *flops* they require. If n is the number of layers, $2m$ the number of data values, and q the nodes in the quadrature formula used to approximate (2.6), we obtain a complexity $O((45n + 8m)q)$ *flops* plus $2nq$ evaluations of functions with a complex argument, and mq with a real argument.

3. Computing the Jacobian matrix. As we will see in the next section, being able to compute or to approximate the Jacobian matrix $J(\boldsymbol{\sigma})$ of the vector function (2.9) is crucial for the implementation of an effective inversion algorithms and to have information about its speed of convergence and conditioning.

The approach used in [15] is to resort to a finite difference approximation

$$\frac{\partial r_i(\boldsymbol{\sigma})}{\partial \sigma_j} = \frac{r_i(\boldsymbol{\sigma} + \boldsymbol{\delta}_j) - r_i(\boldsymbol{\sigma})}{\delta}, \quad i = 1, \ldots, 2m, \ j = 1, \ldots, n, \tag{3.1}$$

where $\boldsymbol{\delta}_j = \delta\, \mathbf{e}_j = (0, \ldots, 0, \delta, 0, \ldots, 0)^T$ and δ is a fixed constant.

In this section we describe the explicit expression of the Jacobian matrix. We will show that the complexity of this computation is smaller than that required by the finite difference approximation (3.1). In the following lemma we omit for clarity the variable λ.

LEMMA 3.1. *The derivatives* $Y'_{kj} = \frac{\partial Y_k}{\partial \sigma_j}$, $k, j = 1, \ldots, n$, *of the surface admittances* (2.2) *can be obtained starting from*

$$Y'_{nn} = \frac{1}{2u_n}, \qquad Y'_{nj} = 0, \quad j = 1, \ldots, n-1, \tag{3.2}$$

and proceeding recursively for $k = n-1, n-2, \ldots, 1$ *by*

$$\begin{aligned} Y'_{kj} &= N_k^2 b_k Y'_{k+1,j}, \qquad j = n, n-1, \ldots, k+1, \\ Y'_{kk} &= \frac{a_k}{2u_k} + \frac{b_k}{2}\left[N_k^2 d_k - Y_{k+1}\left(d_k Y_{k+1} + \frac{1}{\mathrm{i}\mu_k\omega}\right)\right], \\ Y'_{kj} &= 0, \qquad j = k-1, k-2, \ldots, 1, \end{aligned} \tag{3.3}$$

where

$$a_k = \frac{Y_{k+1} + N_k \tanh(d_k u_k)}{N_k + Y_{k+1}\tanh(d_k u_k)}, \quad b_k = \frac{1}{[N_k + Y_{k+1}\tanh(d_k u_k)]^2 \cosh^2(d_k u_k)}. \tag{3.4}$$

Proof. From (2.1) we obtain

$$\frac{\partial u_k}{\partial \sigma_j} = \frac{\partial}{\partial \sigma_j}\sqrt{\lambda^2 + \mathrm{i}\sigma_k\mu_k\omega} = \frac{1}{2N_k}\delta_{kj}, \qquad \frac{\partial N_k}{\partial \sigma_j} = \frac{\partial}{\partial \sigma_j}\frac{u_k}{\mathrm{i}\mu_k\omega} = \frac{1}{2u_k}\delta_{kj}, \tag{3.5}$$

where δ_{kj} is the Kronecker delta, that is 1 if $k = j$ and 0 otherwise. The recursion initialization (3.2) follows from $Y_n = N_n$; see Section 2. We have

$$\begin{aligned} Y'_{kj} = \frac{\partial N_k}{\partial \sigma_j} a_k + N_k \cdot \frac{\frac{\partial Y_{k+1}}{\partial \sigma_j} + \frac{\partial N_k}{\partial \sigma_j}\tanh(d_k u_k) + N_k \frac{\partial \tanh(d_k u_k)}{\partial \sigma_j}}{N_k + Y_{k+1}\tanh(d_k u_k)} \\ - N_k a_k \cdot \frac{\frac{\partial N_k}{\partial \sigma_j} + \frac{\partial Y_{k+1}}{\partial \sigma_j}\tanh(d_k u_k) + Y_{k+1}\frac{\partial \tanh(d_k u_k)}{\partial \sigma_j}}{N_k + Y_{k+1}\tanh(d_k u_k)}, \end{aligned}$$

with a_k defined as in (3.4). If $j \neq k$, then $\frac{\partial N_k}{\partial \sigma_j} = \frac{\partial u_k}{\partial \sigma_j} = 0$ and we obtain

$$Y'_{kj} = N_k^2 \frac{\frac{\partial Y_{k+1}}{\partial \sigma_j}\left(1 - \tanh^2(d_k u_k)\right)}{[N_k + Y_{k+1}\tanh(d_k u_k)]^2} = N_k^2 b_k Y'_{k+1,j}.$$

The last formula, with b_k given by (3.4), avoids the cancellation in $1 - \tanh^2(d_k u_k)$.

If $j = k$, after some straightforward simplifications, we get

$$\begin{aligned} Y'_{kk} = \frac{\partial N_k}{\partial \sigma_k} a_k + \frac{N_k}{N_k + Y_{k+1}\tanh(d_k u_k)}\Big[Y'_{k+1,k}(1 - a_k \tanh(d_k u_k)) \\ + \frac{\partial N_k}{\partial \sigma_k}(\tanh(d_k u_k) - a_k) + \frac{d_k}{2}\left(1 - a_k \frac{Y_{k+1}}{N_k}\right)\left(1 - \tanh^2(d_k u_k)\right)\Big]. \end{aligned}$$

This formula, using (3.4) and (3.5), leads to

$$Y'_{kk} = \frac{a_k}{2u_k} + N_k b_k \left[N_k\left(Y'_{k+1,k} + \frac{d_k}{2}\right) - \frac{1}{2}Y_{k+1}\left(\frac{d_k}{N_k}Y_{k+1} + \frac{1}{u_k}\right)\right].$$

The initialization (3.2) implies that $Y'_{kj} = 0$ for any $j < k$. In particular $Y'_{k+1,k} = 0$, and since N_k/u_k is constant one obtains the expression of Y'_{kk} given in (3.3). This completes the proof. □

REMARK 3.1. The quantity a_k in (3.4) appears in the right hand side of (2.2), and its denominator is present also in b_k. It is therefore possible to implement jointly the recursions (2.2) and (3.3) in order to reduce the number of floating point operations

required by the computation of the Jacobian. We also note that since we only need the partial derivatives of Y_1 in the following Theorem 3.2, we can overwrite the values of $Y'_{k+1,j}$ with Y'_{kj} at each recursion step, so that only n storage locations are needed for each λ value, instead of n^2.

THEOREM 3.2. *The partial derivatives of the residual function* (2.9) *are given by*

$$\frac{\partial r_i(\boldsymbol{\sigma})}{\partial \sigma_j} = \begin{cases} \dfrac{4r}{\mu_0\omega}\mathcal{H}_0\left[\lambda e^{-2h_i\lambda}\,\mathrm{Im}\left(\dfrac{\partial R_0(\lambda)}{\partial \sigma_j}\right)\right](r), & i = 1,\ldots,m, \\ \dfrac{4}{\mu_0\omega}\mathcal{H}_1\left[e^{-2h_{i-n}\lambda}\,\mathrm{Im}\left(\dfrac{\partial R_0(\lambda)}{\partial \sigma_j}\right)\right](r), & i = m+1,\ldots,2m, \end{cases}$$

for $j = 1,\ldots,n$. *Here* $\mathcal{H}_\nu$ ($\nu = 0, 1$) *denotes the Hankel transform* (2.6), r *is the inter-coil distance,* $\frac{\partial R_0(\lambda)}{\partial \sigma_j}$ *is the* j*th component of the gradient of the function* (2.3)

$$\frac{\partial R_0(\lambda)}{\partial \sigma_j} = \frac{-2\mathrm{i}\mu_0\omega\lambda}{(\lambda + \mathrm{i}\mu_0\omega Y_1(\lambda))^2}\cdot\frac{\partial Y_1}{\partial \sigma_j},$$

and the partial derivatives $\frac{\partial Y_1}{\partial \sigma_j}$ *are given by Lemma 3.1.*

Proof. The proof follows easily from Lemma 3.1 and from equations (2.3), (2.5), and (2.7). □

REMARK 3.2. The numerical implementation of the above formulae needs care. It has already been noted in the proof of Lemma 3.1 that equations (3.3)–(3.4) are written in order to avoid cancellations that may introduce huge errors in the computation. Moreover, to prevent overflow in the evaluation of the term

$$\cosh^2(d_k u_k(\lambda)) = \cosh^2(d_k\sqrt{\lambda^2 + \mathrm{i}\sigma_k\mu_k\omega})$$

in the denominator of b_k, we fix a value $\lambda_{\max}$ and for $\mathrm{Re}(d_k u_k(\lambda)) > \lambda_{\max}$ we let $b_k = b_k(\lambda) = 0$. In our numerical experiments we adopt the value $\lambda_{\max} = 300$.

Under the same assumptions assumed at the end of Section 2, we obtain the complexity of the joint computation of the function $\mathbf{r}(\boldsymbol{\sigma})$, defined in (2.9), and its Jacobian, given in Theorem 3.2. It amounts to $O((3n^2 + 8mn)q)$ *flops*, $3nq$ complex functions, and mnq real functions.

To approximate the Jacobian by finite differences, as in (3.1), one has to evaluate $n+1$ times $\mathbf{r}(\boldsymbol{\sigma})$, corresponding to $O((45n^2 + 8mn)q)$ *flops*, $2n^2q$ complex functions, and mnq real functions. It is immediate to observe that the computation of the Jacobian is not more time consuming than its approximation by finite differences, and that for a moderately large n it is much faster to directly compute it, instead than using an approximation.

In order to further reduce the computational cost, it is possible to resort to the *Broyden update* of the Jacobian, which can be interpreted as a generalization of the secant method. Let us denote with $J_0 = J(\boldsymbol{\sigma}_0)$ the Jacobian of the function $\mathbf{r}(\boldsymbol{\sigma})$ computed in the initial point $\boldsymbol{\sigma}_0$. Then, the Broyden update consists of applying the following recursion

$$J_k = J_{k-1} + \frac{(\mathbf{y}_k - J_{k-1}\mathbf{s}_k)\mathbf{s}_k^T}{\mathbf{s}_k^T\mathbf{s}_k}, \tag{3.6}$$

where $\mathbf{s}_k = \boldsymbol{\sigma}_k - \boldsymbol{\sigma}_{k-1}$ and $\mathbf{y}_k = r(\boldsymbol{\sigma}_k) - r(\boldsymbol{\sigma}_{k-1})$. This formula makes the linearization

$$r_k(\boldsymbol{\sigma}) = r(\boldsymbol{\sigma}_k) + J_k(\boldsymbol{\sigma} - \boldsymbol{\sigma}_k)$$

exact in $\boldsymbol{\sigma}_{k-1}$ and guarantees the least change in the Frobenius norm $\|J_k - J_{k-1}\|_F$. The usual approach is to apply recursion (3.6) for $1, \ldots, k_B - 1$, and to recompute the Jacobian after k_B iterations, before reapplying the update, in order to improve accuracy. A single application of (3.6) takes $10mn + 2(m+n)$ *flops*, to be added to the cost of the evaluation of $\mathbf{r}(\boldsymbol{\sigma})$. We will investigate the performance of this method in the numerical experiments.

4. Inversion algorithm. Let the measured data vector $\mathbf{b}$, the model predictions vector $\mathbf{m}(\boldsymbol{\sigma})$, and the residual vector $\mathbf{r}(\boldsymbol{\sigma})$, be defined as in (2.8)–(2.9). The problem of data inversion, which is crucial in order to recover the inhomogeneities of the soil, consists of computing the conductivity σ_i of each layer ($i = 1, \ldots, n$) which determine a given data set $\mathbf{b} \in \mathbb{R}^{2m}$. As it is customary, we use a least squares approach, by solving the nonlinear problem

$$\min_{\boldsymbol{\sigma} \in \mathbb{R}^n} f(\boldsymbol{\sigma}), \qquad f(\boldsymbol{\sigma}) = \frac{1}{2}\|\mathbf{r}(\boldsymbol{\sigma})\|^2 = \frac{1}{2}\sum_{i=1}^{2m} r_i^2(\boldsymbol{\sigma}), \tag{4.1}$$

where $\|\cdot\|$ denotes the Euclidean norm and $r_i(\boldsymbol{\sigma})$ is defined in (2.7).

The vector $\boldsymbol{\sigma}^*$ is a local minimizer of (4.1) if and only if it is a stationary point, i.e., if $\mathbf{f}'(\boldsymbol{\sigma}^*) = 0$, where $\mathbf{f}'(\boldsymbol{\sigma})$ is the gradient of the function f, defined by

$$[\mathbf{f}'(\boldsymbol{\sigma})]_j = \frac{\partial f(\boldsymbol{\sigma})}{\partial \sigma_j} = \sum_{i=1}^{2m} r_i(\boldsymbol{\sigma}) \frac{\partial r_i(\boldsymbol{\sigma})}{\partial \sigma_j}, \qquad j = 1, \ldots, n; \tag{4.2}$$

see, e.g., [2] for a complete treatment. We assume that f is differentiable and smooth enough that the following Taylor expansion

$$\mathbf{f}'(\boldsymbol{\sigma} + \mathbf{s}) = \mathbf{f}'(\boldsymbol{\sigma}) + \mathbf{f}''(\boldsymbol{\sigma})\mathbf{s} + O(\|\mathbf{s}\|^2) \simeq \mathbf{f}'(\boldsymbol{\sigma}) + \mathbf{f}''(\boldsymbol{\sigma})\mathbf{s}$$

is valid for $\|\mathbf{s}\|$ sufficiently small, where

$$[\mathbf{f}''(\boldsymbol{\sigma})]_{jk} = \frac{\partial^2 f(\boldsymbol{\sigma})}{\partial \sigma_j \partial \sigma_k} = \sum_{i=1}^{2m} \left(\frac{\partial r_i(\boldsymbol{\sigma})}{\partial \sigma_j} \frac{\partial r_i(\boldsymbol{\sigma})}{\partial \sigma_k} + r_i(\boldsymbol{\sigma}) \frac{\partial^2 r_i(\boldsymbol{\sigma})}{\partial \sigma_j \partial \sigma_k} \right) \tag{4.3}$$

is the Hessian of the function f.

Newton's method chooses the step $\mathbf{s}_\ell$ by imposing that $\boldsymbol{\sigma}^*$ is a stazionary point, i.e., as the solution to

$$\mathbf{f}''(\boldsymbol{\sigma}_\ell)\mathbf{s}_\ell = -\mathbf{f}'(\boldsymbol{\sigma}_\ell).$$

The next iterate is then computed as $\boldsymbol{\sigma}_{\ell+1} = \boldsymbol{\sigma}_\ell + \mathbf{s}_\ell$. The analytic expression of the Hessian $\mathbf{f}''(\boldsymbol{\sigma})$ is not always available; whenever it is, its computation implies a large computational cost. To overcome this problem, one possibility is to resort to the Gauss–Newton method, which is based on the solution of a sequence of linear approximations of $\mathbf{r}(\boldsymbol{\sigma})$, rather than of $\mathbf{f}'(\boldsymbol{\sigma})$.

Let $\mathbf{r}$ be Fréchet differentiable and $\boldsymbol{\sigma}_k$ denote the current approximation, then we can write

$$\mathbf{r}(\boldsymbol{\sigma}_{k+1}) \simeq \mathbf{r}(\boldsymbol{\sigma}_k) + J(\boldsymbol{\sigma}_k)\mathbf{s}_k,$$

where $\boldsymbol{\sigma}_{k+1} = \boldsymbol{\sigma}_k + \mathbf{s}_k$ and $J(\boldsymbol{\sigma})$ is the Jacobian of $\mathbf{r}(\boldsymbol{\sigma})$, defined by

$$[J(\boldsymbol{\sigma})]_{ij} = \frac{\partial r_i(\boldsymbol{\sigma})}{\partial \sigma_j}, \qquad i = 1, \ldots, 2m,\ j = 1, \ldots, n.$$

At each step k, $\mathbf{s}_k$ is the solution of the linear least squares problem

$$\min_{\mathbf{s} \in \mathbb{R}^n} \|\mathbf{r}(\boldsymbol{\sigma}_k) + J_k \mathbf{s}\|, \tag{4.4}$$

where $J_k = J(\boldsymbol{\sigma}_k)$ or some approximation; see, e.g., (3.1) and (3.6).

Problem (4.4) is equivalent to the normal equation

$$J_k^T J_k \mathbf{s} = -J_k^T \mathbf{r}(\boldsymbol{\sigma}_k), \tag{4.5}$$

from which we obtain the following iterative method

$$\boldsymbol{\sigma}_{k+1} = \boldsymbol{\sigma}_k + \mathbf{s}_k = \boldsymbol{\sigma}_k - J_k^\dagger \mathbf{r}(\boldsymbol{\sigma}_k), \tag{4.6}$$

where $J_k^\dagger$ is the Moore–Penrose pseudoinverse of J_k [2]; if $2m \geq n$ and J_k has full rank, then $J_k^\dagger = (J_k^T J_k)^{-1} J_k^T$. Using this notation, the gradient (4.2) and the Hessian (4.3) of $f(\boldsymbol{\sigma})$ can be written as

$$\begin{aligned} \mathbf{f}'(\boldsymbol{\sigma}) &= J(\boldsymbol{\sigma})^T \mathbf{r}(\boldsymbol{\sigma}), \\ \mathbf{f}''(\boldsymbol{\sigma}) &= J(\boldsymbol{\sigma})^T J(\boldsymbol{\sigma}) + \sum_{i=1}^{2m} r_i(\boldsymbol{\sigma}) H_i(\boldsymbol{\sigma}), \end{aligned} \tag{4.7}$$

where

$$[H_i(\boldsymbol{\sigma})]_{jk} = \frac{\partial^2 r_i(\boldsymbol{\sigma})}{\partial \sigma_j \partial \sigma_k}$$

is the Hessian of the ith residual $r_i(\boldsymbol{\sigma})$. Then, the Gauss–Newton method (4.6) can be seen as a special case of Newton's method, obtained by neglecting the term $\sum_{i=1}^{2m} r_i(\boldsymbol{\sigma}) H_i(\boldsymbol{\sigma})$ from (4.7). This term is small if either each $r_i(\boldsymbol{\sigma})$ is mildly nonlinear at $\boldsymbol{\sigma}_k$, or the residuals $r_i(\boldsymbol{\sigma}_k)$, $i = 1, ..., 2m$, are small. Since we are focused on the nonlinear case, we do not take into account the first assumption. We remark that in the case of a mildly nonlinear problem, a linear model is available [3, 18].

When the residuals $r_i(\boldsymbol{\sigma}_k)$ are small, or when the problem is consistent ($\mathbf{r}(\boldsymbol{\sigma}^*) = 0$), the Gauss–Newton method can be expected to behave similarly to Newton's method. In particular, the local convergence rate will be quadratic for both methods. If the above conditions are not satisfied, the Gauss–Newton method may not converge. We remark that, while the physical problem is obviously consistent, this is not necessarily true in our case, since we assume a layered soil, that is, we approximate the conductivity $\sigma(z)$ by a piecewise constant function. Furthermore, in the presence of noise in the data the problem will certainly be inconsistent.

To ensure convergence, the damped Gauss–Newton method replaces the approximation (4.6) by

$$\boldsymbol{\sigma}_{k+1} = \boldsymbol{\sigma}_k + \alpha_k \mathbf{s}_k, \tag{4.8}$$

where α_k is a step length to be determined. To choose it, we used the Armijo–Goldstein principle [19], which selects α_k as the largest number in the sequence 2^{-i}, $i = 0, 1, \ldots$, for which the following inequality holds

$$\|\mathbf{r}(\boldsymbol{\sigma}_k)\|^2 - \|\mathbf{r}(\boldsymbol{\sigma}_k + \alpha_k \mathbf{s}_k)\|^2 \geq \frac{1}{2}\alpha_k \|J_k \mathbf{s}_k\|^2.$$

The damped method allows us to include an important physical constraint in the inversion algorithm, i.e., the positivity of the solution. In our implementation α_k is the largest step size which both satisfies the Armijo–Goldstein principle and ensures that all the solution components are positive.

As we will show in the following section, the problem is severely ill-conditioned, so regularization is needed.

5. Regularization methods. To investigate the conditioning of problem (4.1), we studied the behaviour of the singular values of the Jacobian matrix $J = J(\boldsymbol{\sigma})$ of the vector function $\mathbf{r}(\boldsymbol{\sigma})$. Let $J = U\Gamma V^T$ be the singular value decomposition (SVD) [2] of the Jacobian, where U and V are orthogonal matrices of size $2m$ and n, respectively, $\Gamma = \mathrm{diag}(\gamma_1, \ldots, \gamma_p, 0, \ldots, 0)$ is the diagonal matrix of the singular values, and p is the rank of J; its condition number is then given by γ_1/γ_p.

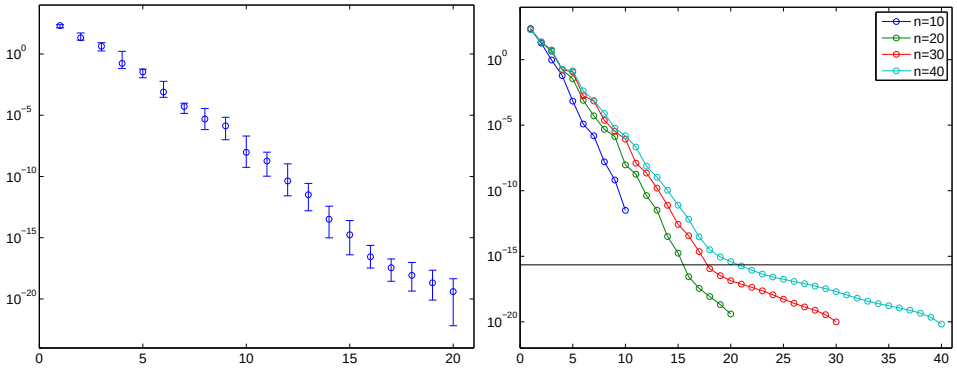

FIG. 5.1. *SVD of the Jacobian matrix: left, average singular values and errors ($n = 20$); right, average singular values for $n = 10, 20, 30, 40$.*

Fixed $m = 10$, we generate randomly 1000 vectors $\boldsymbol{\sigma} \in \mathbb{R}^{20}$, having components in $[0, 100]$. For each of them we evaluate the correponding Jacobian $J(\boldsymbol{\sigma})$ by the formulae proved in Theorem 3.2 and compute its SVD. The left graph in Figure 5.1 shows the average of the singular values obtained by the above procedure and, for each of them, its minimum and maximum value. It is clear that deviation from the average is small, so that the condition number of the Jacobian matrix has of the same order of magnitude in all tests. Consequently, the linearized problem is severely ill-conditioned independently of the value of $\boldsymbol{\sigma}$, and we do not expect its condition number to change much during iteration.

The right graph in Figure 5.1 reports the average singular values when $n = 2m = 10, 20, 30, 40$. The figure shows that the condition number is about 10^{14} when $n = 10$ and increases with dimension. The singular values appear to be exponentially decaying, so the problem is not strictly rank-deficient. The decay rate of singular values appears to change below machine precision $2.2 \cdot 10^{16}$, which is represented in the graph by a horinzontal line. The exact singular vales are likely to decay with a

stronger rate while the computed ones, reported in the graph, are probably strongly perturbated by error propagation. A problem of this kind is generally referred to as a *discrete ill-posed problem* [11], so regularization is needed.

A typical approach for the solution of ill-posed problems is Tikhonov regularization. It has been applied by various author to the inversion of geophysical data; see, e.g., [3, 6, 15]. To apply Tikhonov's method to the nonlinear problem (4.1), one has to solve the minimization problem

$$\min_{\boldsymbol{\sigma}\in\mathbb{R}^{\mathbf{n}}} \{\|\mathbf{r}(\boldsymbol{\sigma})\|^2 + \mu^2 \|L\boldsymbol{\sigma}\|^2\} \tag{5.1}$$

for a fixed value of the parameter μ, where L is a regularization matrix; L is often chosen as the identity matrix, or a discrete approximation of the first or second derivative. When the variance of the noise in the data is known, the regularization parameter μ is usually chosen by the discrepancy principle, otherwise various heuristic methods are used; see [11]. The available methods to estimate the parameter require the computation of the regularized solution $\boldsymbol{\sigma}_\mu$ of (5.1) for many values of μ. This can be done, for example, by the Gauss–Newton method, leading to a a large computational effort.

To reduce the complexity we consider an alternative regularization technique based a low-rank approximation of the Jacobian matrix. The best rank ℓ approximation ($\ell \le p$) to the Jacobian according to the Euclidean norm, i.e., the matrix A_ℓ which minimizes $\|J - A\|$ over all the matrices of rank ℓ, can be easily obtained by the above SVD decomposition $J = U\Gamma V$. This procedure allows us to replace the ill-conditioned Jacobian matrix with a well-conditioned rank-deficient matrix A_ℓ. The corresponding solution to (4.4) is known as the truncated SVD (TSVD) solution [10] and can be expressed as

$$\mathbf{s}^{(\ell)} = -A_\ell^\dagger \mathbf{r} = -\sum_{i=1}^{\ell} \frac{\mathbf{u}_i^T \mathbf{r}}{\gamma_i} \mathbf{v}_i, \tag{5.2}$$

where $\ell = 1, \ldots, p$ is the regularization parameter, γ_i are the singular values, the singular vectors $\mathbf{u}_i$ and $\mathbf{v}_i$ are the orthogonal columns of U and V, respectively, and $\mathbf{r} = \mathbf{r}(\boldsymbol{\sigma}_k)$.

To introduce a regularization matrix $L \in \mathbb{R}^{t\times n}$ ($t \le n$), problem (4.4) is usually replaced by

$$\min_{\mathbf{s}\in\mathcal{S}} \|L\mathbf{s}\|, \qquad \mathcal{S} = \{\mathbf{s} \in \mathbb{R}^n \ : \ J^T J\mathbf{s} = -J^T\mathbf{r}\}, \tag{5.3}$$

under the assumption $\mathcal{N}(J) \cap \mathcal{N}(L) = \{0\}$. The generalized singular value decomposition (GSVD) [20] of the matrix pair (J, L) is the factorization

$$J = U\Sigma_J Z^{-1}, \qquad L = V\Sigma_L Z^{-1},$$

where U and V are orthogonal matrices and Z is nonsingular. The general form of the diagonal matrices Σ_J and Σ_L, having the same size of J and L, is more complicated than we need, so we analyze two cases we are interested in. In the case $2m \ge n = p$, the two diagonal matrices are given by

$$\Sigma_J = \begin{bmatrix} 0 & 0 \\ C & 0 \\ 0 & I_{n-t} \end{bmatrix}, \qquad \Sigma_L = \begin{bmatrix} S & 0 \end{bmatrix},$$

where I_{n-t} is the identity matrix of size $n-t$ and

$$C = \mathrm{diag}(c_1, \ldots, c_t), \qquad S = \mathrm{diag}(s_1, \ldots, s_t),$$

with $c_i^2 + s_i^2 = 1$. The diagonal elements are ordered such that the *generalized singular values* $\gamma_i = c_i/s_i$ are nondecresing with $i = 1, \ldots, t$. When $p = 2m < n$, we have

$$\Sigma_J = \begin{bmatrix} 0 & C & 0 \\ 0 & 0 & I_{n-t} \end{bmatrix}, \qquad \Sigma_L = \begin{bmatrix} I_{n-2m} & 0 & 0 \\ 0 & S & 0 \end{bmatrix},$$

where C and S are diagonal matrices of size $2m-n+t$. The positivity of this number poses a constraint on the size of L.

The truncated GSVD (TGSVD) solution $\mathbf{s}_\ell$ to (5.3) is then defined as

$$\mathbf{s}^{(\ell)} = -\sum_{i=\overline{p}-\ell+1}^{\overline{p}} \frac{\mathbf{u}_{2m-p+i}^T \mathbf{r}}{c_i} \mathbf{z}_{n-p+i} - \sum_{i=\overline{p}+1}^{p} (\mathbf{u}_{2m-p+i}^T \mathbf{r})\, \mathbf{z}_{n-p+i}, \tag{5.4}$$

where $\ell = 0, 1, \ldots, \overline{p}$ is the regularization parameter, $\overline{p} = t$ if $2m \geq n$ and $\overline{p} = 2m-n+t$ if $2m < n$.

Our approach to construct a regularized solution to (4.1) consists of regularizing each step of the damped Gauss-Newton method (4.8) by either TSVD or TGSVD. For a fixed value of the regularization parameter ℓ, we substitute $\mathbf{s}$ in (4.8) by $\mathbf{s}^{(\ell)}$ expressed by either (5.2) or (5.4). We let the resulting method

$$\boldsymbol{\sigma}_{k+1}^{(\ell)} = \boldsymbol{\sigma}_k^{(\ell)} + \alpha_k \mathbf{s}_k^{(\ell)} \tag{5.5}$$

iterate until

$$\|\boldsymbol{\sigma}_k^{(\ell)} - \boldsymbol{\sigma}_{k-1}^{(\ell)}\| < \tau \|\boldsymbol{\sigma}_k^{(\ell)}\| \quad \text{or} \quad k > 100 \quad \text{or} \quad \alpha_k < 10^{-5},$$

for a given tolerance τ. The constraint on α_k is due to its role in ensuring the positivity of the solution. Indeed, when the solution blows up because of ill-conditioning the damping parameter assumes very small values. We denote the solution at convergence by $\boldsymbol{\sigma}^{(\ell)}$. We will discuss the choice of ℓ in the next subsection.

5.1. Choice of the regularization parameter. In the previous Section we saw how to regularize the ill-conditioned problem (4.1) with the aid of T(G)SVD. The choice of the regularization parameter is crucial in order to obtain a good approximation $\boldsymbol{\sigma}^{(\ell)}$ of $\boldsymbol{\sigma}$. In this work we make use of some well-known methods to choose a suitable index ℓ.

In real-world applications experimental data are always affected by noise. To model this situation, we assume that the data vector in the residual function (2.9), whose norm is minimized in problem (4.1), can be expressed as $\mathbf{b} = \widehat{\mathbf{b}} + \mathbf{e}$, where $\widehat{\mathbf{b}}$ contains the exact data and $\mathbf{e}$ is the noise vector. This vector is generally assumed to have normally distributed entries with mean zero and common variance.

If an accurate estimate of the norm of the error $\mathbf{e}$ in $\mathbf{b}$ is known, the value of ℓ can often be determined with the aid of the discrepancy principle [7, Section 4.3]. It consists of determining the regularization parameter ℓ as the smallest index $\ell = \ell_{\mathrm{discr}}$ such that

$$\|\mathbf{b} - \mathbf{m}(\boldsymbol{\sigma}_{\ell_{\mathrm{discr}}})\| \leq \kappa \|\mathbf{e}\|. \tag{5.6}$$

Here $\kappa > 1$ is a user-supplied constant independent of $\|\mathbf{e}\|$. In our experiments we set $\kappa = 1.5$, since it produced the best numerical results. The discrepancy principle typically yields a suitable truncation index when an accurate bound for $\|\mathbf{e}\|$ is available.

We are also interested in the situation when an accurate bound for $\|\mathbf{e}\|$ is not available and, therefore, the discrepancy principle cannot be applied. A large number of methods for determining a regularization parameter in this situation have been introduced for linear inverse problems [11]. They are known as *heuristic* because it is not possible to prove convergence results for them, in the strict sense of the definition of a regularization method; see, e.g., [7, Chapter 4]. Nevertheless, it has been shown by numerical experiments, that some heuristic methods provide a good estimation of the optimal regularization parameter in many inverse problems of applicative interest.

It is not possible, in general, to apply all the heuristic methods, which were developed in the linear case, to a nonlinear problem. In this paper we use the L-curve criterion [14], which can be extended quite naturally to the nonlinear case. Let us consider the curve obtained by joining the points

$$\left\{ \log \|\mathbf{r}(\boldsymbol{\sigma}^{(\ell)})\|, \log \|L\boldsymbol{\sigma}^{(\ell)}\| \right\}, \quad \ell = 1, \ldots, \overline{p},$$

where $\mathbf{r}(\boldsymbol{\sigma}^{(\ell)}) = \mathbf{b} - \mathbf{m}(\boldsymbol{\sigma}^{(\ell)})$ is the residual error associated to the approximate solution $\boldsymbol{\sigma}^{(\ell)}$ computed by the iterative method (5.5), using (5.4) as a regularization method. If (5.2) is used instead, it is sufficient to let $L = I$ and replace $\overline{p}$ by p.

This curve exhibits a typical L-shape in many discrete ill-posed problems. The L-curve criterion seeks to determine the regularization parameter by detecting the index ℓ of the point of the curve closer to the corner of the "L". This choice produces a solution for which both the norm and the residual are fairly small.

Various method has been proposed to determine the corner of the L-curve. In our numerical experiments we use two of them. The first one, which we denote as the *corner* method, considers a sequence of pruned L-curves, obtained by removing an increasing number of points, and constructs a list of candidate vertices produced by two different selection algorithms. The corner is selected from this list by a procedure which compares the norms and the residuals of the corresponding solutions [13]. It is currently implemented in [12].

The second procedure we use has been recently proposed in [23], by extending a method by T. Regińska [22], which detects the corner by solving an optimization problem. We will refer to this method as the *restricted Regińska* (ResReg) method.

6. Numerical experiments. To illustrate the performance of the inversion methods described in the previous sections we present here the results of a set of numerical experiments. Initially, we will apply our method to synthetic data sets, generated by choosing a conductivity distribution and adding random noise to data. Finally, we will analyze a real data set.

Figure 6.1 reports the three functions $f_\ell(z)$, $\ell = 1, 2, 3$, used in our experiments to model the distribution of conductivity, expressed in Siemens/meter, with respect to the depth z, measured in meters. The first one is differentiable ($f_1(z) = \mathrm{e}^{-(z-1)^2}$), the second is piecewise linear, the third is a step function. All model functions assume the presence of a strongly conductive material at a given depth.

For a chosen model function f_k and a fixed number of layers n, we let the layers thickness assume the constant value $d_k = \bar{d} = 2/(n-1)$, $k = 1, \ldots, n-1$ (see Section 2), so that $z_j = (j-1)\bar{d}$, $j = 1, \ldots, n$. The choice of $\bar{d}$ is motivated by the

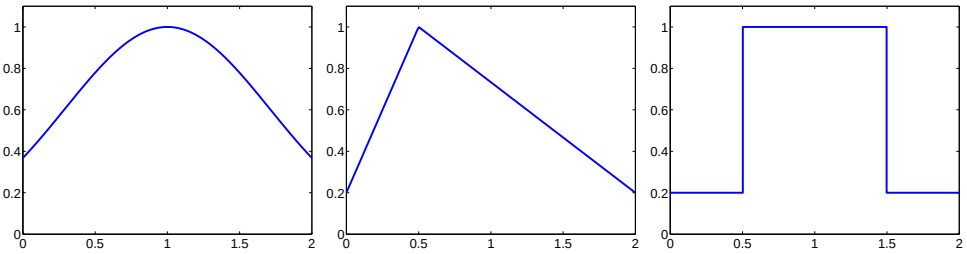

FIG. 6.1. *Graphs of the conductivity distribution models f_1, f_2, and f_3. The horizontal axis reports the depth in meters, the vertical axis the electrical conductivity in Siemens/meter.*

common assumption that a GCM can give useful information about the conductivity of the ground up to a depth of 2 meters. This fact is confirmed by our experiments.

We assign to each layer the conductivity $\sigma_j = f_k(z_j)$. Then, we apply the nonlinear model (2.8) to compute the exact data vector $\widehat{\mathbf{b}}$, letting

$$\widehat{b}_i = \begin{cases} \hat{b}_i^V = m^V(\boldsymbol{\sigma}, h_i), & i = 1, \ldots, m, \\ \hat{b}_{m-i}^H = m^H(\boldsymbol{\sigma}, h_{m-i}), & i = m+1, \ldots, 2m. \end{cases}$$

We assume that the measurements are taken with the EMS in both vertical and horizontal orientation, placed at the heights $h_i = (i-1)\bar{h}$ above the ground, $i = 1, \ldots, m$, for a chosen height step $\bar{h}$; see (2.7). In our experiments $\bar{h} \geq 0.1$m.

To simulate experimental errors, we determine the perturbed data vector $\mathbf{b}$ by adding a noise vector to $\widehat{\mathbf{b}}$. Specifically, we let the vector $\mathbf{w}$ have normally distributed entries with mean zero and variance one, and compute

$$\mathbf{b} = \widehat{\mathbf{b}} + \mathbf{w}\, \|\widehat{\mathbf{b}}\| \frac{\tau}{\sqrt{2m}}.$$

This implies that $\|\mathbf{b} - \widehat{\mathbf{b}}\| \approx \tau \|\widehat{\mathbf{b}}\|$. In the computed examples we use the noise levels $\tau = 10^{-3}, 10^{-2}, 10^{-1}$. The value of τ is used in the discrepancy principle (5.6), where we substitute $\tau \|\widehat{\mathbf{b}}\|$ for $\|\mathbf{e}\|$.

For each data set, we solve the least squares problem (4.1) by the damped Gauss–Newton method (4.8). The damping parameter is determined by the Armijo–Goldstein principle, modified in order to ensure the positivity of the solution. Each step of the iterative method is regularized by either the TSVD approach (5.2), or by TGSVD (5.4), for a given regularization matrix L. In our experiments we use both $L = D_1$ and $L = D_2$, the discrete approximations of the first and second derivatives. This two choices pose a constraint on the magnitude of the slope and the curvature of the solution, respectively. To assess the accuracy of the computations we use the relative error

$$e_\ell = \frac{\|\boldsymbol{\sigma} - \boldsymbol{\sigma}^{(\ell)}\|}{\|\boldsymbol{\sigma}\|}, \tag{6.1}$$

where $\boldsymbol{\sigma}$ denotes the exact solution of the problem and $\boldsymbol{\sigma}^{(\ell)}$ its regularized solution with parameter ℓ, obtained by (5.5). The experiments were performed using Matlab 8.1 (R2013a) on an Intel Core i7/860 computer with 8Gb RAM, running Linux. The software developed is available from the authors upon request.

TABLE 6.1

Optimal error e_{opt} for $m = 5, 10, 20$ and $n = 20, 40$, for the TSVD solution ($L = I$) and the TGSVD solution with $L = D_1$ and $L = D_2$. The Jacobian is computed as in Section 3.

		$L = I$		$L = D_1$		$L = D_2$	
example	m	$n = 20$	$n = 40$	$n = 20$	$n = 40$	$n = 20$	$n = 40$
f_1	5	2.4e-01	2.4e-01	8.6e-02	8.0e-02	6.9e-02	7.0e-02
	10	2.2e-01	2.1e-01	5.2e-02	5.7e-02	5.2e-02	4.6e-02
	20	2.2e-01	2.2e-01	3.9e-02	4.9e-02	3.1e-02	3.5e-02
f_2	5	3.1e-01	3.7e-01	7.2e-02	6.4e-02	9.7e-02	1.2e-01
	10	2.8e-01	3.5e-01	6.3e-02	6.2e-02	7.3e-02	8.2e-02
	20	2.8e-01	3.9e-01	6.5e-02	5.9e-02	7.9e-02	7.2e-02
f_3	5	4.2e-01	4.6e-01	2.9e-01	2.9e-01	2.9e-01	3.0e-01
	10	3.5e-01	4.7e-01	2.7e-01	2.6e-01	2.7e-01	2.8e-01
	20	3.3e-01	4.7e-01	2.6e-01	2.6e-01	2.7e-01	2.9e-01

Our first experiment tries to determine the optimal experimental setting, that is, the number of measurements to be taken and the number of underground layers to be considered. At the same time, we investigate the difference between the TSVD (5.2) and the TGSVD (5.4) approaches, and the effect on the solution of the regularization matrix L. For each of the three test conductivity models, we discretize the soil by 20 or 40 layers, up to the depth of 2m. We generate synthetic measures at 5, 10, and 20 equispaced heights up to 1.9m, and we solve the problem. This process is repeated for each regularization matrix. The (exact) Jacobian is computed as described in Section 3. Table 6.1 reports the values of the relative error $e_{\text{opt}} = \min_\ell e_\ell$, representing the best possible performance of the method. This value is the average over 20 realizations of the noise.

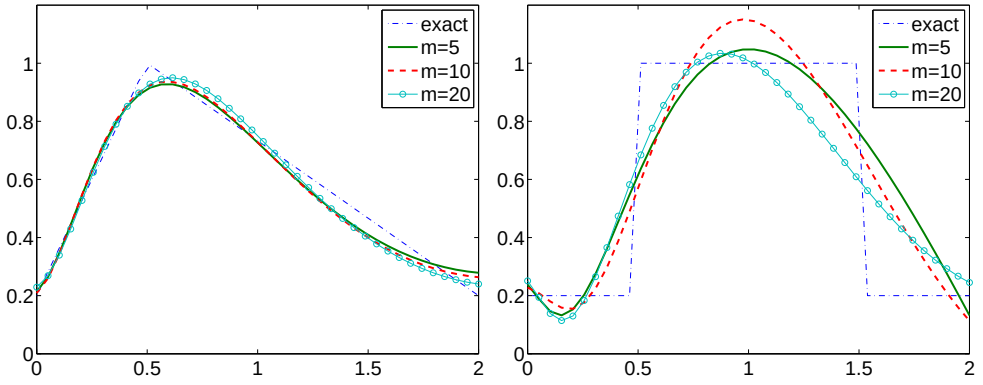

FIG. 6.2. *Optimal reconstruction for the model functions f_2 and f_3. The number of underground layers is $n = 40$, the noise level is $\tau = 10^{-3}$. The solid line is the solution obtained with $m = 5$, the dashed line corresponds to $m = 10$, the line with bullets to $m = 20$. The exact solution is represented by a dash-dotted line.*

It is clear that the TSVD approach is the least accurate. The TGSVD with $L = D_2$ gives the best results for f_1, that is when the solution is smooth. When the conductivity distribution is less regular, like f_2 and f_3, the first derivative $L = D_1$ produces the more accurate approximations. From the results, it seems convenient to use a large number of layers to discretize the soil, that is $n = 40$. This choice

TABLE 6.2

Optimal error e_{opt} for $m = 5, 10, 20$ and $n = 20, 40$, for f_1 ($L = D_2$), f_2 ($L = D_1$), and f_3 ($L = D_1$). The results obtained from measurements collected with the instrument in both vertical and horizontal orientation are compared to those obtained with a single orientation.

		f_1, $L = D_2$		f_2, $L = D_1$		f_3, $L = D_1$	
orientation	m	$n = 20$	$n = 40$	$n = 20$	$n = 40$	$n = 20$	$n = 40$
both	5	6.9e-02	7.0e-02	7.2e-02	6.4e-02	2.9e-01	2.9e-01
	10	5.2e-02	4.6e-02	6.3e-02	6.2e-02	2.7e-01	2.6e-01
	20	3.1e-02	3.5e-02	6.5e-02	5.9e-02	2.6e-01	2.6e-01
vertical	5	1.4e-01	1.0e-01	1.8e-01	1.8e-01	3.7e-01	3.7e-01
	10	7.0e-02	1.2e-01	1.4e-01	1.4e-01	3.8e-01	3.5e-01
	20	7.5e-02	7.5e-02	1.2e-01	1.1e-01	3.3e-01	3.3e-01
horizontal	5	1.3e-01	1.3e-01	2.7e-01	2.6e-01	4.4e-01	4.1e-01
	10	8.4e-02	6.1e-02	1.4e-01	1.2e-01	3.8e-01	4.0e-01
	20	7.2e-02	6.7e-02	1.1e-01	8.6e-02	3.5e-01	3.4e-01

does not increase significantly the computation time. It is obviously desirable to have at disposal a large number of measurements, however the results obtained with $m = 5$ and $m = 10$ are not much worse than those computed with $m = 20$, and they might be sufficient to give a rough approximation of the depth localization of a conductive substance. This is an important remark, as it reduces the time needed for data acquisition.

Figure 6.2 gives an idea of the quality of the computed reconstructions for the model functions f_2 and f_3, with $n = 40$ and noise level $\tau = 10^{-3}$. The exact solution is compared to the approximations corresponing to $m = 5, 10, 20$. The above remarks about the influence of the number of measurements m is confirmed. It is also remarkable that the position of the maximum is very well localized.

In the previous experiments we assumed that all the $2m$ entries of vector $\mathbf{b}$ in (2.8) were available. In Table 6.2 we compare these results with those obtained by using only half of them, i.e., those corresponding to either the vertical or horizontal orientation of the instrument. The results with the label "both" in the first column are extracted from Table 6.1. The results are slightly worse when the number of data is halved, especially for the smooth model function, while they are almost equivalent for the step function f_3.

In Section 3 we described the computation of the Jacobian matrix of (2.9), and compared it to the slower finite difference approximation (3.1) and to the Broyden update (3.6). To investigate the execution time corresponding to each method, we let the method (5.5) perform 100 iterations, with $L = D_2$, for a fixed regularization parameter ($\ell = 4$). When the Jacobian is exactly computed, the execution time is 7.18s, while the finite difference approximation requires 18.96s. The speedup factor is 2.6, which is far less than the one theoretically expected. This is probably due to the implementation details, and to the fact that the Matlab programming language is interpreted. We performed the same experiment by applying the Broyden update (3.6) and recomputing the Jacobian every k_B iterations. For $k_B = 5$ the execution time was 2.00s, for $k_B = 10$, 1.32s. Despite this strong speedup, the accuracy is not substantially affected by this approach. Table 6.3 reports the relative error e_{opt} obtained by repeating the experiment of Table 6.1 using the Broyden method with $k_B = 10$. We only report the values of e_{opt} for the most interesting examples. The loss of accuracy is minimal.

TABLE 6.3

Optimal error e_{opt} for $m = 5, 10, 20$ and $n = 20, 40$, for f_1 ($L = D_2$), f_2 ($L = D_1$), and f_3 ($L = D_1$). The Jacobian is computed every 10 iterations and then updated by the Broyden method.

	f_1, $L = D_2$		f_2, $L = D_1$		f_3, $L = D_1$	
m	$n = 20$	$n = 40$	$n = 20$	$n = 40$	$n = 20$	$n = 40$
5	7.3e-02	7.6e-02	7.7e-02	7.6e-02	3.0e-01	2.9e-01
10	5.5e-02	4.8e-02	6.9e-02	7.4e-02	2.7e-01	2.8e-01
20	4.3e-02	4.0e-02	7.3e-02	6.9e-02	2.6e-01	2.7e-01

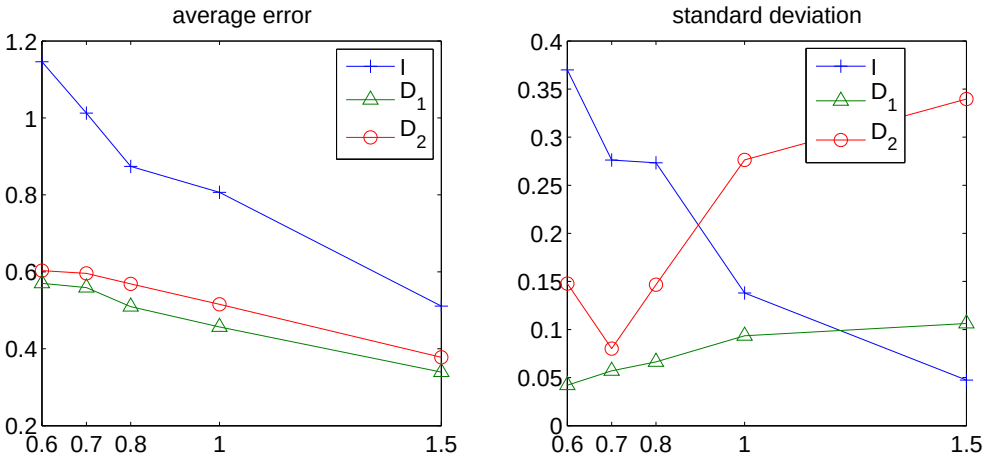

FIG. 6.3. *Results for the reconstruction of test function f_3 with a variable step length ξ, which is reported on the horizontal axis. The left graph reports the average error e_{opt}, obtained with three regularization matrices $L = I, D_1, D_2$. Each test is repeated 20 times for each noise level $\tau = 10^{-3}, 10^{-2}, 10^{-1}$. The right graph reports the corresponding standard deviations.*

Another interesting issue is understanding which is the spatial resolutions of the inversion algorithm, that is, which is the performance of the method in the presence of a very thin conductive layer. To this end, we consider the test function f_3, and let the length ξ of the step vary. Each problem is solved for three regolarization matrices, three noise levels, and each test is repeated 20 times for different noise realizations. The left graph of Figure 6.3 reports the average errors for each value of ξ, while the right graph displays the standard deviations. The choice $L = D_1$ appears to be the best. Indeed, not only the errors are better, but the smaller standard deviations ensure that the method is more reliable. Figure 6.4 shows the reconstructions of f_3 with three different step lengths, with $\xi = 1.5, 1.0, 0.7$, $L = D_1$, and $\tau = 10^{-2}$. It is remarkable that the position of the maximum is well located by the algorithm even in the presence of a very thin step.

REFERENCES

[1] W. L. Anderson. Numerical integration of related Hankel transforms of orders 0 and 1 by adaptive digital filtering. *Geophysics*, 44(7):1287–1305, 1979.

[2] Å. Björck. *Numerical Methods for Least Squares Problems*. SIAM, Philadelphia, 1996.

[3] B. Borchers, T. Uram, and J. M. H. Hendrickx. Tikhonov regularization of electrical conductivity depth profiles in field soils. *Soil Science Society of America Journal*, 61(4):1004–1009, 1997. Package LINEM38 available at `http://infohost.nmt.edu/~borchers/linem38.html`.

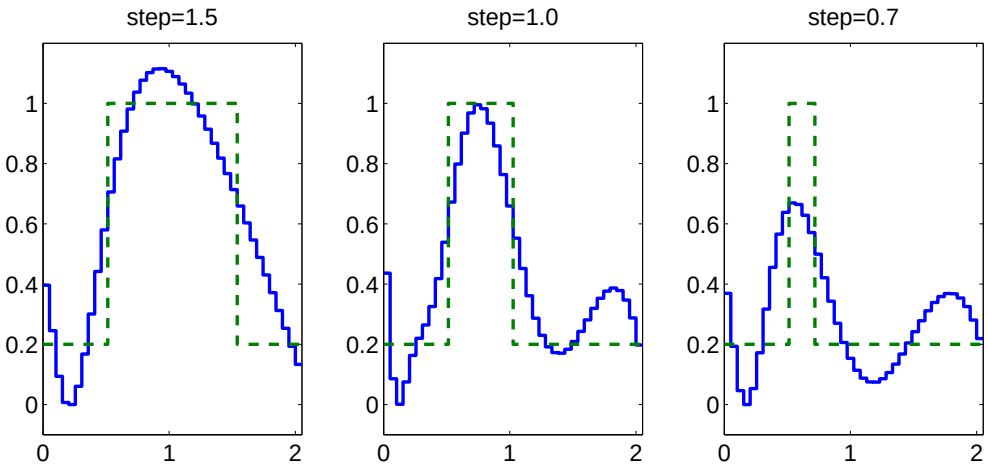

FIG. 6.4. *Optimal reconstructions for the test function f_3, with step lengths 1.5, 1.0, and 0.7, obtained with $L = D_1$ and noise level $\tau = 10^{-2}$.*

[4] J. B. Callegary, T. Ferré, and R. W. Groom. Vertical spatial sensitivity and exploration depth of low-induction-number electromagnetic-induction instruments. *Vadose Zone Journal*, 6(1):158–167, 2007.

[5] D. L. Corwin and S. M. Lesch. Characterizing soil spatial variability with apparent soil electrical conductivity: I. survey protocols. *Computers and Electronics in Agriculture*, 46(1):103–133, 2005.

[6] G. P. Deidda, E. Bonomi, and C. Manzi. Inversion of electrical conductivity data with Tikhonov regularization approach: some considerations. *Annals of Geophysics*, 46(3):549–558, 2003.

[7] H. W. Engl, M. Hanke, and A. Neubauer. *Regularization of Inverse Problems*. Kluwer, Dordrecht, 1996.

[8] D. C. Fraser and G. Hodges. Induction-response functions for frequency-domain electromagnetic mapping system for airborne and ground configurations. *Geophysics*, 72(2):F35–F44, 2007.

[9] R. Gebbers, E. Lück, and K. Heil. Depth sounding with the EM38-detection of soil layering by inversion of apparent electrical conductivity measurements. *Precision Agriculture*, 7:95–102, 2007.

[10] P. C. Hansen. The truncated SVD as a method for regularization. *BIT*, 27:543–553, 1987.

[11] P. C. Hansen. *Rank-Deficient and Discrete Ill-Posed Problems, Numerical Aspects of Linear Inversion*. SIAM, Philadelphia, PA, 1998.

[12] P. C. Hansen. Regularization Tools: Version 4.0 for Matlab 7.3. *Numer. Algorithms*, 46:189–194, 2007.

[13] P. C. Hansen, T. K. Jensen, and G. Rodriguez. An adaptive pruning algorithm for the discrete L-curve criterion. *J. Comput. Appl. Math.*, 198(2):483–492, 2007.

[14] P. C. Hansen and D. P. O'Leary. The use of the l-curve in the regularization of discrete ill-posed problems. *SIAM J. Sci. Comput.*, 14:1487–1503, 1993.

[15] J. M. H. Hendrickx, B. Borchers, D. L. Corwin, S. M. Lesch, A. C. Hilgendorf, and J. Schlue. Inversion of soil conductivity profiles from electromagnetic induction measurements. *Soil Science Society of America Journal*, 66(3):673–685, 2002. Package NONLINEM38 available at `http://infohost.nmt.edu/~borchers/nonlinem38.html`.

[16] S. M. Lesch, D. J. Strauss, and J. D. Rhoades. Spatial prediction of soil salinity using electromagnetic induction techniques: 1. statistical prediction models: A comparison of multiple linear regression and cokriging. *Water Resources Research*, 31(2):373–386, 1995.

[17] H. P. Martinelli and A. M. Osella. Small-loop electromagnetic induction for environmental studies at industrial plants. *Journal of Geophysics and Engineering*, 7(1):91, 2010.

[18] J. D. McNeill. Electromagnetic terrain conductivity measurement at low induction numbers. Technical Report TN-6, Geonics Limited, Mississauga, Ontario, Canada, 1980.

[19] J. M. Ortega and W. C. Rheinboldt. *Iterative Solution of Nonlinear Equations in Several Variables*. Academic Press, 1970.

[20] C. C. Paige and M. A. Saunders. Towards a generalized singular value decomposition. *SIAM*

J. Numer. Anal., 18(3):398–405, 1981.

[21] J. G. Paine. Determining salinization extent, identifying salinity sources, and estimating chloride mass using surface, borehole, and airborne electromagnetic induction methods. *Water Resources Research*, 39(3), 2003.

[22] T. Regińska. A regularization parameter in discrete ill-posed problems. *SIAM J. Sci. Comput.*, 17:740–749, 1996.

[23] L. Reichel and G. Rodriguez. Old and new parameter choice rules for discrete ill-posed problems. *Numer. Algorithms*, 63(1):65–87, 2013.

[24] J. Van Der Kruk, J. A. C. Meekes, P. M. Van Den Berg, and J. T. Fokkema. An apparent-resistivity concept for low-frequency electromagnetic sounding techniques. *Geophysical Prospecting*, 48(6):1033–1052, 2000.

[25] J. R. Wait. *Geo-Electromagnetism*. Academic Press, New York, 1982.

[26] R. Yao and J. Yang. Quantitative evaluation of soil salinity and its spatial distribution using electromagnetic induction method. *Agricultural Water Management*, 97(12):1961–1970, 2010.